Controlled Preferential Oxidation of Grain Boundaries in Monolayer Tungsten Disulfide for Direct Optical Imaging

Youmin Rong, Kuang He, Mercè Pacios, Alex W. Robertson, Harish Bhaskaran, and Jamie H. Warner*

Department of Materials, University of Oxford, Parks Road, Oxford, OX1 3PH, United Kingdom

ABSTRACT Synthetic 2D crystal films grown by chemical vapor deposition are typically polycrystalline, and determining grain size within domains and continuous films is crucial for determining their structure. Here we show that grain boundaries in the 2D transition metal dichalcogenide WS_2, grown by CVD, can be preferentially oxidized by controlled heating in air. Under our developed conditions, preferential degradation at the grain boundaries causes an increase in their physical size due to oxidation. This increase in size enables their clear and rapid identification using a standard optical microscope. We demonstrate that similar treatments in an Ar environment do no show this effect, confirming that oxidation is the main role in the structural change. Statistical analysis of grain boundary (GB) angles shows dominant mirror formation. Electrical biasing across the GB is shown to lead to changes at the GB and their observation under an optical microscope. Our approach enables high-throughput screening of as-synthesized WS_2 domains and continuous films to determine their crystallinity and should enable improvements in future CVD growth of these materials.

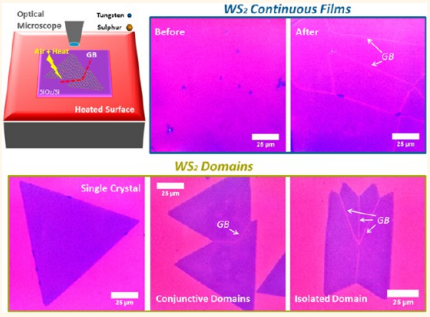

KEYWORDS: WS_2 · grain boundaries · 2D crystals · TMDs · 2D materials

Development of chemical vapor deposition (CVD) techniques has enabled the growth of large-scale high-quality two-dimensional (2D) materials such as single-atom-thick graphene.[1−4] However, grain boundaries (GBs) in the as-synthesized 2D films are easily formed due to the merger of randomly oriented crystalline domains during the growth of the polycrystalline films.[5,6] The GBs play an important role in influencing electron transport properties.[4,7−10] Therefore, there is an urgent need for not only realizing lateral GB distributions across a given sized sample but also being able to detect them on a large scale and in a time-efficient manner. GBs in graphene have been extensively imaged and studied at the atomic scale using transmission electron microscopy (TEM)[11,12] or scanning tunneling microscopy (STM).[7,13,14] This approach is limited to studying only small regions of the sample and was substantially improved in terms of the through-put and area examined by using optical microscopy for graphene GBs directly on copper. This was achieved by a straightforward moisture-rich oxidation of the sample.[15]

Recent advancement in CVD for producing two-dimensional metal dichalcogenide (TMD) domains and thin films over large areas[16−20] and application of these 2D TMDs in optical studies[21−24] and optoelectronics[25−28] have promoted the need for determining their grain boundaries. GBs and grain structures of monolayer MoS_2 have been successfully examined using a color-coded overlay of dark-field-TEM images.[8] GBs in WS_2 domains on sapphire substrates were made partially visible by scanning electron microscopy (SEM) using mild oxidation under moisture-rich ambient conditions, taking up to 20 days to emerge.[29] However, this was a random process with no control and took excessively long for GBs to emerge as visible. Several parts of the WS_2 domains also showed deterioration, making the unambiguous assignment of the GBs challenging. Recent work has shown that UV exposure

* Address correspondence to Jamie.warner@materials.ox.ac.uk.

Received for review October 14, 2014 and accepted April 10, 2015.

Published online April 14, 2015
10.1021/acsnano.5b00852

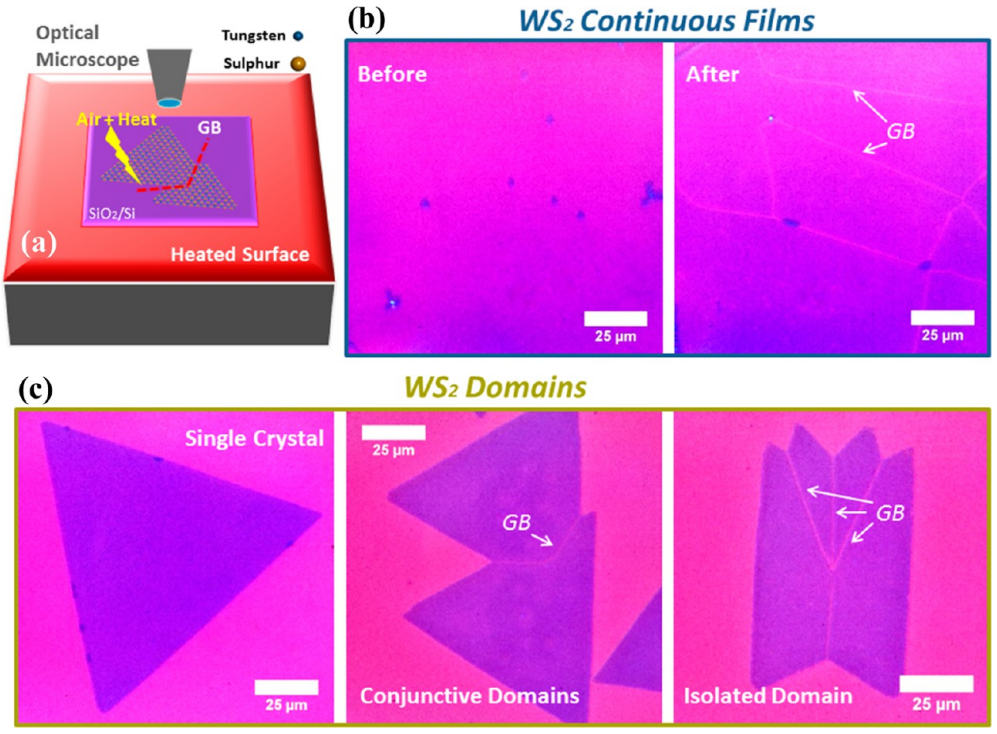

Figure 1. Grain boundaries revealed in monolayer WS_2 continuous films and crystalline domains using the as-developed thermal treatment in air (380 °C for 20 min) and observed by an optical microscope. (a) Schematic illustration of the thermal treatment that enabled direct imaging of WS_2 GBs using an optical microscope. (b) Optical images of a monolayer WS_2 continuous film before and after the thermal treatment in air, resulting in the appearance of WS_2 GBs. (c) Optical images of WS_2 GBs in other monolayer configurations of the as-formed WS_2 crystal, which can be generally summarized as single crystal, conjunctive domains, and isolated domain.

leads to deterioration of the GBs in TMDs, and it is likely that this is the driving cause of GB deterioration when TMDs are left in room light and in air.[30] The GBs of the 2D materials are not easily detectable using optical microscopy because of their nanometer-sized widths.[16−18,31,32] An approach to reveal GBs in 2D TMDs directly on as-deposited substrates with rapid throughput time using large-area examination methods such as imaging by optical microscopy is still important.

RESULTS AND DISCUSSION

Here we demonstrate a reproducible rapid technique for revealing GBs in CVD-grown monolayer WS_2 domains and continuous films on SiO_2/Si substrates under a standard optical microscope. This controlled approach relies on simple heating in air to cause preferential structural changes localized on the WS_2 GBs, shown schematically in Figure 1a. High-quality CVD growth of TMDs provides isolated domains that can grow from between 20 and 400 μm. However, detecting the size of the grains within TMD continuous films has been limited due to the absence of suitable techniques that can detect the GBs on the micro- to millimeter scale. We have improved our recently reported CVD approach to enable control of either isolated domains or continuous film growth of WS_2 monolayers (see supporting Figure S1). This gives us the ability to probe both types of TMD crystal forms: isolated single crystals and polycrystalline films. Raman spectroscopy and photoluminescence spectroscopy confirmed that both the isolated domains and the continuous films are predominantly monolayer (supporting Figure S2). We explored several heating conditions to reach the conclusion that 20 min at 380 °C provided both rapid transformation and achieving a clear GB appearance. Figure 1b and c show that before heat treatment there are no lines of contrast, but after heat treatment strong contrast lines associated with GBs appear in the WS_2. For isolated WS_2 domains there are several shapes grown during the CVD. In Figure 1c we show the results from heating a perfect triangular-shaped domain, most likely a single crystal, and then two multifaceted structures, likely formed from several crystals merging together. Multifaceted WS_2 domains after heat treatment show strong contrast lines in locations where one would expect GBs to have formed based on the faceted structures. In contrast, the single-crystal triangle in Figure 1c does not show any contrast lines after heat treatment, which provides a strong indication that the contrast lines are GBs. The heat treatment of the continuous films shows similar strong contrast lines, and we can extrapolate from our findings that these lines are the GBs in these films.

We used selected area electron diffraction (SAED) within a TEM to map out the crystal structure within

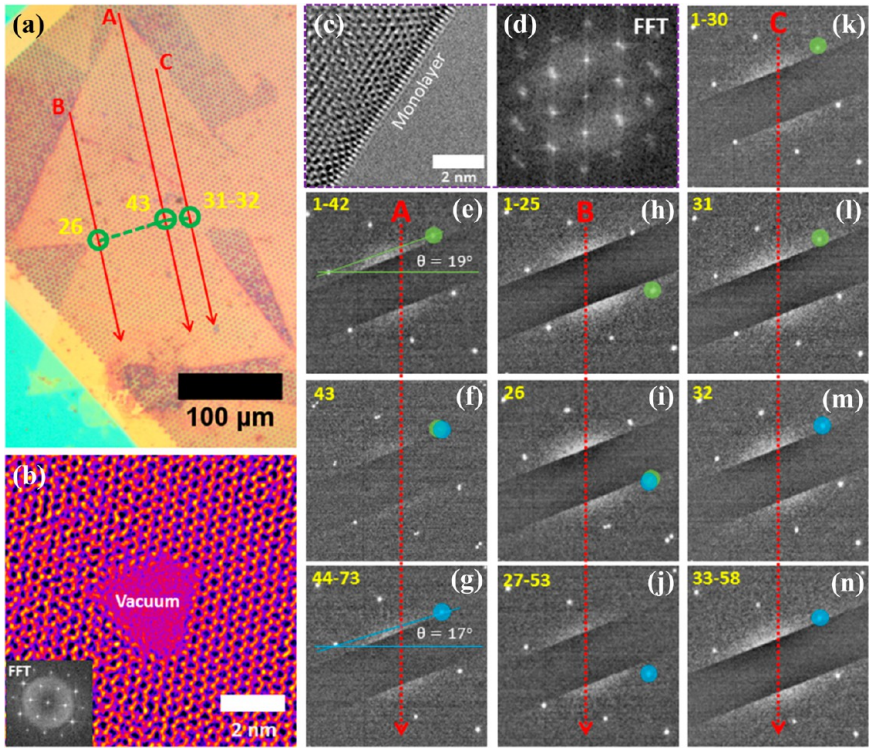

Figure 2. TEM characterizations of monolayer WS_2 domains with regard to the GB locations and crystallinity performed on a holey SiN TEM grid. (a) Optical microscopy image of a WS_2 domain transferred onto the SiN TEM grid with highlighted (red) hole arrays (A, B, and C) for SAED characterizations. Green circles indicate as-determined WS_2 GB positions across the domain with highlighted numbered holes for corresponding SAED diffractions patterns in (f), (i), (l), and (m), respectively. (b) Aberration-corrected (AC)-TEM image of the WS_2 domain showing a hexagonal lattice structure with a hole created by an electron beam to show it is a monolayer, and the corresponding FFT pattern is introduced in the inset (a color look-up-table of "Fire" is used to improve visual inspection). (c) Smoothed AC-TEM image taken on the back-folded edge of a monolayer WS_2 with part (d) showing its corresponding FFT image. (e−g) SAED diffraction patterns taken from the hole array A, which spans from hole number 1 to 73. (h−j) SAED patterns obtained from hole number 1 to 53 of the hole array B. (k−n) Hole number 1 to 58 SAED patterns acquired from the hole array C. The corresponding WS_2 crystal orientations relative to the horizontal level are presented in (e) and (g) as 19° in green and 17° in blue, respectively, which also applies to the color coding in parts (h) to (n). This SiN TEM grid has a hole-center to adjacent hole-center distance of 4.5 μm.

two connected monolayer WS_2 domains transferred onto a holey SiN TEM grid, Figure 2. A hole was introduced into the WS_2 using the 80 kV electron beam, and the atomic resolution image taken by an aberration-corrected TEM, Figure 2b, shows the hole opens to vacuum, confirming it is monolayer thickness. Examination of the back-folded WS_2 edge also shows only a single line of contrast, expected for folded monolayer 2D materials, Figure 2c. Taking SAED patterns from each hole provides accurate tracking of the crystal orientation and reveals a grain boundary running through locations A43 and B26 and between C31 and C32 (Figure 2e−n). The as-transferred WS_2 domain has only two crystal orientations across approximately ~324 μm (see supporting Figure S3). This confirms our findings in Figure 1. Another example of GB mapping by SAED measurements also confirms the findings, supporting Figure S4.

We have carried out an extensive study of how heating temperature in air over time affects the appearance of WS_2 GBs under optical microscopy (as demonstrated in supporting Figure S5). Figure 3a depicts the unveiling of GBs in monolayer WS_2 domains after 90 min exposure to a heating temperature of 250 °C in air. If the heating temperature is lower than 250 °C, in our study, the GBs in WS_2 domains are not observable with optical microscopy after 90 min. On the other hand, the efficiency of this particular approach can be much improved by having a higher heating temperature, as shown in Figure 3b. By treating the WS_2 domains at 380 °C in air, the amount of time needed for GBs to be visible by optical microscope can be shortened to 20 min. This provided a pathway for more time-efficient GB imaging of monolayer WS_2 domains or films in this context. Further increase in the heating temperature or prolongation of the treatment can eventually result in damaging the crystal domains, instead allowing GBs to only mildly develop (supporting Figure S6), and makes the unambiguous identification of GBs challenging. In addition to the control of the heating temperature, the environment in which to process monolayer WS_2 domains or films is also of great importance. Figure 3c demonstrates that using the same heating temperature and the same duration as in Figure 3b but processing instead in an Ar atmosphere led to failure in observing

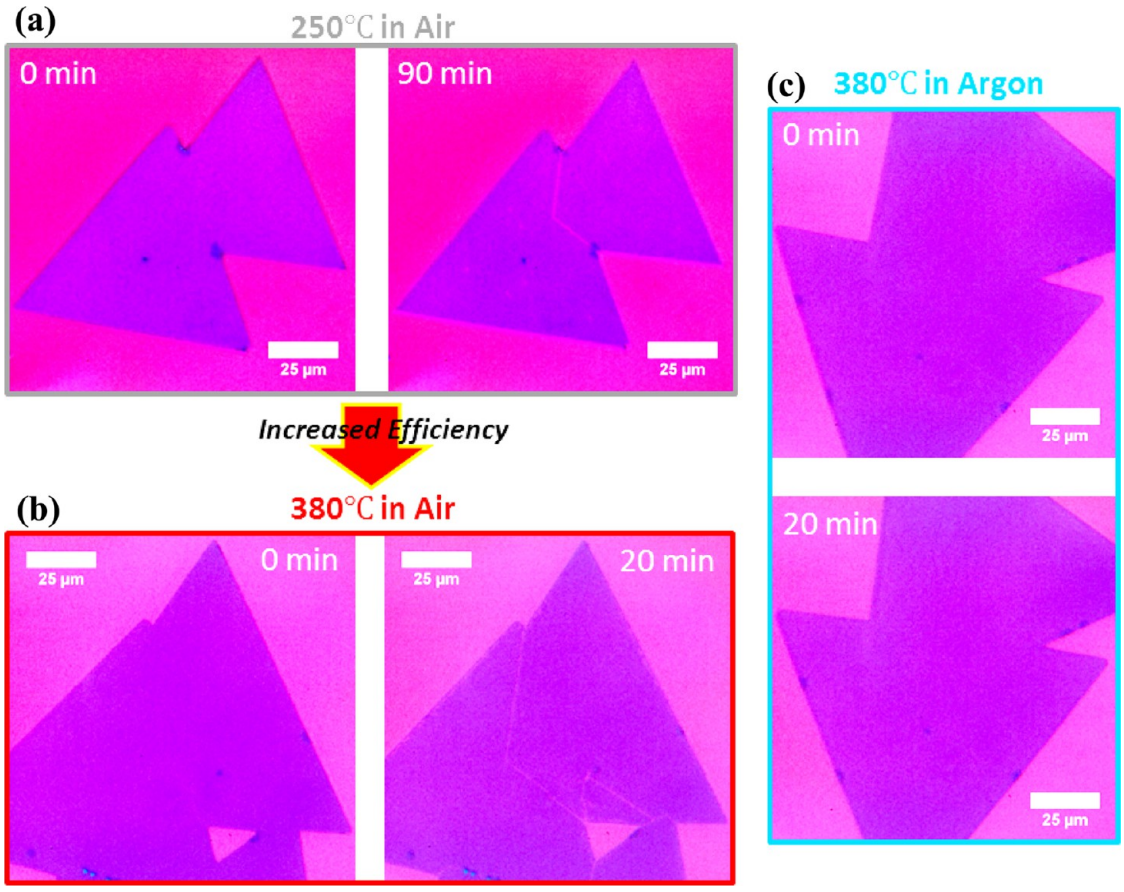

Figure 3. Optical images of WS_2 domains showing the effect of time and heating temperature in air or in an inert argon atmosphere on GB visualization. (a) Before and after 90 min in air at a heating temperature of 250 °C. (b) Before and after 20 min in air at a heating temperature of 380 °C. (c) Before and after 20 min in argon at a heating temperature of 380 °C.

WS_2 GBs optically. This reveals that the thermal treatment for the GB imaging of monolayer WS_2 domains with optical microscopy should be done in an oxidizing environment.

Raman spectroscopy and photoluminescence (PL) spectroscopy were used to probe the GBs after the heat treatment, Figure 4. Figure 4a shows that there is a small decrease in PL peak intensity of the bulk region of the treated WS_2 domains compared to the pristine domains. Moreover, the PL emission of the GBs of the treated WS_2 shows nearly a 2-fold decrease in signal relative to that of the central part of the treated domains. Thermal treatment with air may cause adsorption of O_2/H_2O from the air or defect creation due to applied thermal energy at WS_2 GBs, which may result in either PL enhancement[33,34] or quenching.[8,29] We have found only a small peak shift of 1 nm between the pristine and treated WS_2 domains. We were also able to detect the WS_2 GBs from a PL map of a treated domain, Figure 4b (*i.e.*, PL mapping was generated by plotting integrated PL peak intensities against XY coordinates where multipoint PL analysis was carried in that specific area of the WS_2 domain). Raman spectroscopy and 2D Raman mapping can also detect changes of crystallinity either in monolayer WS_2 domains or in GBs after heating in air at the designated temperature, Figure 4c–f. The pristine and treated WS_2 domains show similar monolayer characteristic Raman profiles of WS_2 with an in-plane vibrational (E^1_{2g}) mode of ~351 cm^{-1} and an out-of-plane vibrational (A_{1g}) mode of ~418 cm^{-1}, with no peak shifting or quenched intensities observed.[35] For the treated WS_2 GBs, the intensity of E^1_{2g} and A_{1g} peaks were reduced by 2-fold as compared to the central part of the treated WS_2 domains (and pristine WS_2 domains). Similar to the PL mapping of WS_2 GBs, both E^1_{2g} and A_{1g} peak intensities from the treated GBs can be used in 2D Raman mapping to see the GBs, Figure 4d and e. In addition, the WS_2 GBs after the treatment can also be mapped out using the ratio of E^1_{2g} to A_{1g}, Figure 4f. Without heating the WS_2 domains, as we have done, PL and Raman 2D mappings cannot clearly reveal the GBs (supporting Figure S7).[17,29]

GBs in as-produced high-quality CVD monolayer WS_2 domains and polycrystalline films are difficult to detect even under SEM, Figure 5a. However, in certain cases of CVD growth of 2D TMD crystals, some contrast can be detected from the GBs under SEM[29,36] or optical microscopy[10,32] due to unwanted multilayer crystal growth or contamination, as shown in the case of

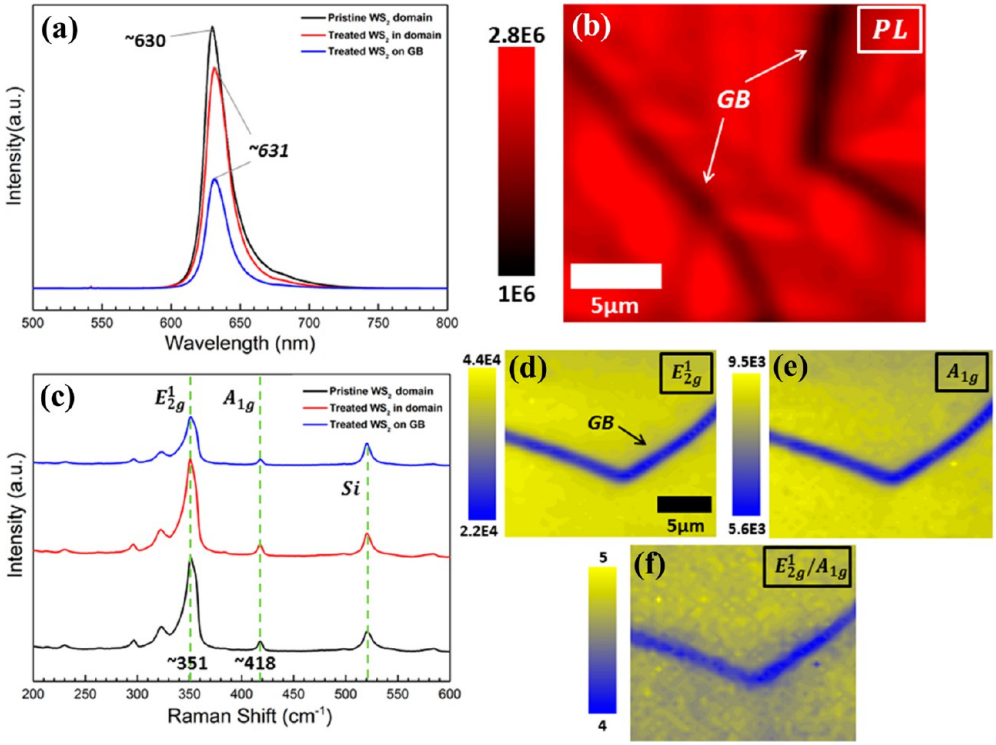

Figure 4. PL and Raman characterizations for as-treated monolayer WS_2 domains at a 532 nm excitation laser. (a) PL emission profiles obtained in a pristine monolayer WS_2 domain as opposed to the treated monolayer WS_2 on a GB or in a domain. (b) PL 2D mapping of the as-developed WS_2 GBs according to the integrated characteristic photon emission intensities from wavelengths of 600 to 660 nm. (c) Raman spectra obtained in a pristine monolayer WS_2 domain in comparison with the treated monolayer WS_2 on a GB or in a domain, with highlighted Si peak and WS_2 characteristic peaks, E^1_{2g} and A_{1g}. (d) Raman 2D mapping of the WS_2 GBs with regard to the integrated characteristic E^1_{2g} peak intensities from 330 to 370 cm^{-1}. (e) Raman mapping of the WS_2 GBs executed for the A_{1g} characteristic peak with integrated intensities from 400 to 430 cm^{-1}. (f) Raman mapping of the WS_2 GBs corresponding to the ratio of integrated E^1_{2g} peak intensities (330−370 cm^{-1})/integrated A_{1g} peak intensities (400−430 cm^{-1}).

Figure 5b.[10,36] After our controlled heat treatment in air, a strong contrast (blisters) from the GBs in SEM (Figure 5c) may arise from balling of as-formed WO_x in the GB defect area due to reduction of surface energy. Atomic force microscopy (AFM) revealed that the GBs increased in width after heating in air, Figure 5d−i. The actual width of the GB after heating, Figure 5g, is approximately 0.55 μm, Figure 5i, which is large enough to be detected under an optical microscope.[15]

The ability to measure the GBs in a large number of WS_2 domains under an optical microscope enabled a statistical study of their relative orientation with respect to the WS_2 triangle orientation. We found that mirror GBs (*i.e.*, GB formed at half-angle (θ) of the two neighboring domain zigzag edges (α)) dominated (Figure 6a). Figure 6b plots the α/θ ratio distribution for 100 GBs measured in oxidized-treated joined domains, fitted with the Lorentz curve (red). In Figure 6c, typical optical images of GBs are shown, emphasizing that the α/θ ratio is mostly 2. The creation of GB defects occurs when one single crystal merges with another single crystal of different orientation (Figure 6d,e). While the GBs may appear straight at the microscopic level, previous work using STEM has shown that mirror GBs predominantly consist of eight- and four-membered rings at the atomic level in MoS_2 (Figure 6e).[8,37] Given that the mirror GBs form for all domains, regardless of their initial relative orientation and separation of domain centers, it is likely that the mirror GBs do not represent the region where the two domains initially meet and connect, but rather that the system reconstructs after two domains merge together and the GBs adjust until reaching the mirror symmetry.

The large size of the CVD-grown WS_2 domains enables electrical contacts using sharp W probes in a probe station brought directly into the crystals without any lithography needed and thus reduces contamination. Figure 7a and b show the typical *IV* electrical properties of the as-grown WS_2 domain as well as domains that were oxidized in air. Probes were placed in specified regions likely to be the same crystal to ensure no grain boundary would lie in-between the probes. Both pristine and heat-treated WS_2 domains are conductive at an applied source−drain bias of 10 V onward (*i.e.*, a current compliance of 500 nA was used to avoid excess current, which heats the sample and causes irreversible deterioration). The W probes form a Schottky barrier with the WS_2 and result in a nonlinear *IV* curve and large onset bias voltage. The similar *IV*

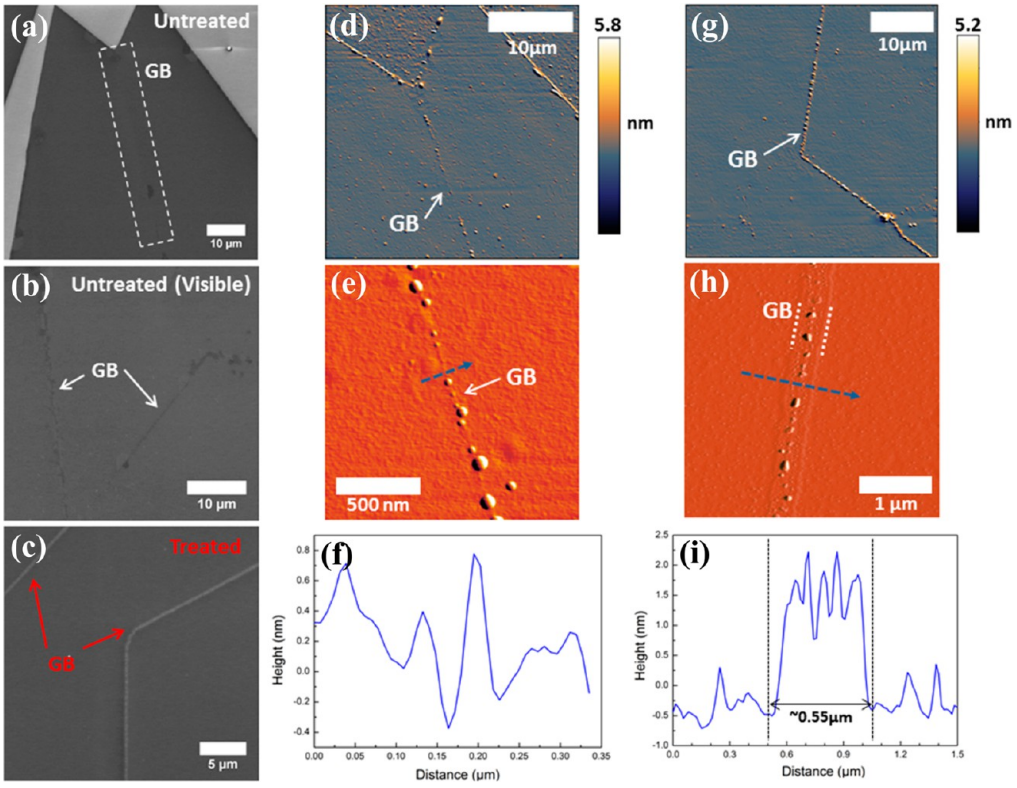

Figure 5. Topological characterizations of the treated WS_2 GBs using SEM and AFM. (a) Untreated WS_2 GBs that are invisible under the SEM observation. (b) Untreated WS_2 GBs that are partially visible with SEM. (c) Treated WS_2 GBs that show strong contrast with SEM. (d) AFM topological mapping of the untreated WS_2 GB. (e) Close-up mapping of the untreated WS_2 GB. (f) Corresponding line profile indicated (blue) in (e). (g) AFM topological mapping of the as-treated WS_2 GBs. (h) Finer AFM mapping specifically carried out for determination of the topology within the as-treated WS_2 GBs. (i) As-obtained topological line profile indicated (blue) in (h).

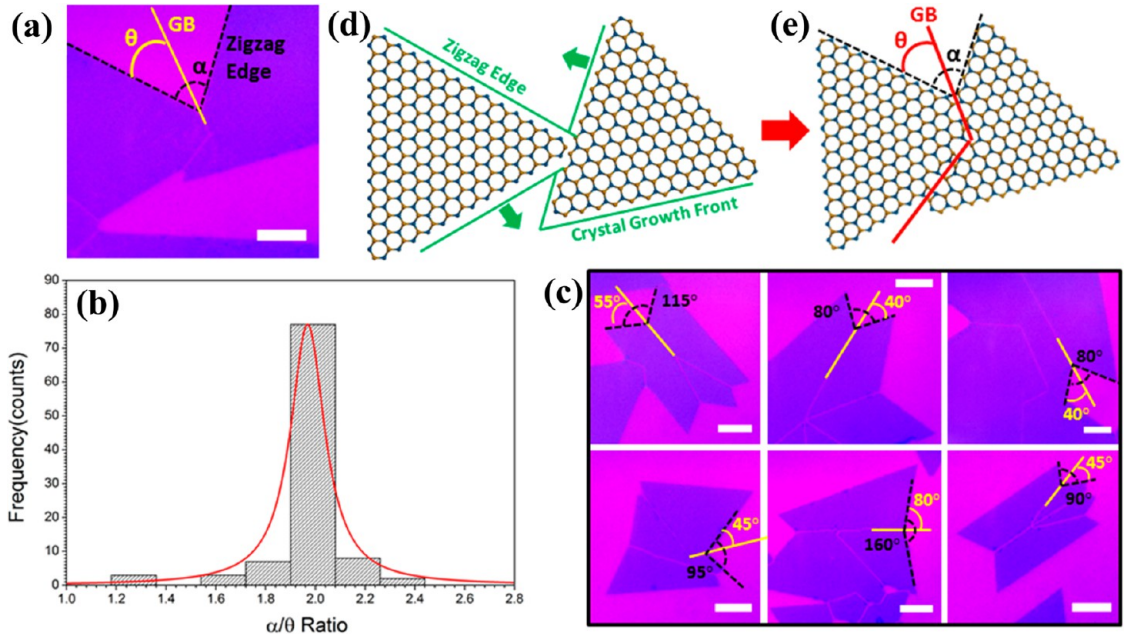

Figure 6. Preferential GB orientations incurred from mismatching of as-grown monolayer WS_2 domains. (a) Schematic illustration of GB angle (θ = angle between the GB and the neighboring domain edge) bisecting the domain angle (α = angle between two neighboring zigzag edges). Scale bar = 20 μm. (b) Domain angle (α)/GB angle (θ) ratio distribution in 100 monolayer WS_2 domains obtained from our CVD approach. (c) Optical images showing that the majority of GB θ angles bisect the domain α angles in as-synthesized WS_2 joined domains (all scale bars are 20 μm). (d) Schematic illustration of two pristine WS_2 triangular single crystals with zigzag edges merging together to form a GB. (e) Schematic atomic model showing the formation of a GB structure at an orientation that bisects the domain edge angle.

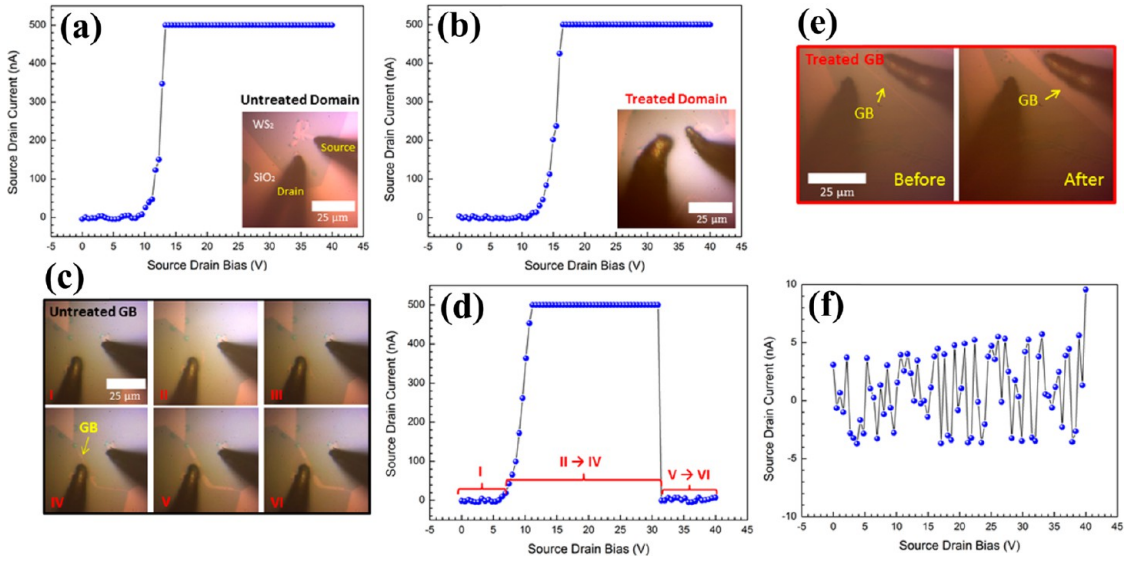

Figure 7. *IV* **source−drain electrical measurements of monolayer WS_2 against its domain (or GB) that is pristine and heat-treated, respectively. (a, b) Output $I_{sd}V_{sd}$ curves of an as-grown WS_2 domain that is unprocessed and processed by heat treatment in air, respectively. (c) Optical images I to VI showing an untreated WS_2 GB being revealed under optical microscope at elevated source−drain biases applied against the pristine GB. (d) Corresponding output profile of the untreated WS_2 GB appearing in (c). (e) Optical images showing before and after applying source−drain bias against a thermally treated WS_2 GB. (f) Corresponding output profile of the WS_2 GB presented in (e). All measurements were conducted at a source−drain-bias increase rate of approximately 1.24 V/s.**

response of the WS_2 before and after oxidization shows that the material conductivity of the WS_2 domain after heat treatment was not greatly affected by the mild oxidation.

Electrical measurements were then taken across a GB for the as-grown WS_2 domains by placing the probe tips on either side of a GB. Upon applying the bias, current started to flow, as in the case of the non-GB area, but surprisingly, the GB started to emerge visibly under the optical microscope after a period of current flow, shown in the sequence of images in Figure 7c. The optically invisible GB junction at two domains was found vulnerable to further increase of source−drain bias until the two domains became fully separated at the GB site. The corresponding *IV* measurement shown in Figure 7d monitors how the level of current across the WS_2 GB increases at first (source−drain bias stages I to IV), but then drops suddenly to zero when the source−drain bias reaches ~30 V and remains zero for further ramping of the source−drain bias (stages V to VI). This correlates in the optical images of Figure 7c to the increase of the WS_2 GB width, resulting in the formation of two isolated WS_2 domains with no current flowing between. To further study this, W probes were placed on either side of a GB made visible by the heat-treatment process in WS_2 and bias was applied to monitor the *IV* response. Figure 7e and f show that no current flows across the oxidized GB as the bias is increased, but that the width of the GB increases substantially after ramping the bias up to 40 V (as in Figure 7c). Another identical example is provided in supporting Figure S8. We repeated these measurements on more than 100 domains and found qualitatively consistent behavior.

These results show not only that controlled heat treatment of WS_2 domains can lead to the GB becoming visible under the optical microscope through an oxidization process but also that applying a relatively large bias also causes the GB to become visible. During the biasing across a GB, current flows, causing heating that instigates an oxidization process in the more reactive area of the GB, similar to the heat-treatment process we developed. This is important when considering the operation of WS_2-based field effect transistors in air where similar effects might occur if current levels are high. If we limit current flow across the GB by implementing a severe compliance value (*i.e.*, 10 nA), then this GB degradation does not occur, indicating that it is related to some form of joule heating and not driven by the electric field alone. On the other hand, the increase of the GB width in Figure 7e results from heat localization in the W tip area rather than at the GB area. When current does not flow in between a GB, a leaking current through the SiO_2 substrate (large resistance) will generate heat to that WS_2 region, resulting in further oxidation of the WS_2 domain close to the GB.

CONCLUSION

The combination of diffraction mapping, optical imaging, Raman and PL mapping, and AFM has revealed that simply heating WS_2 domains in air at the right temperature for a short 20 min burst causes the GBs to increase and be observed using a standard

optical microscope. This demonstrates that the grain boundary, which is known to contain defects, has a lower oxidation reaction temperature than the bulk crystal. The process works for both domains and polycrystalline films, is high-throughput and large-area, and does not require any fancy equipment for preparation. The ease of this approach should enable its uptake across the community for TMD 2D materials to provide a robust way of determining the degree of polycrystallinity of continuous large-area films and can be implemented on the centimeter scale. Knowing the grain size of TMD films will help correlations between electronic performance and structure and should lead to the rapid improvement of continuous TMD films by CVD growth, which is critical to their further development in optoelectronics.

METHODS

CVD Synthesis of Monolayer WS_2. The monolayer WS_2 domains and continuous films were fabricated by adopting the sulfur preintroduction protocols recently reported by Rong *et al.*[17] However, rather having sulfur and WO_3 precursors placed in the same tube, we optimized the system by separating them using a double-walled-quartz-tube CVD setup (supporting Figure S1). This has successfully prevented sulfur vapor from reacting with WO_3 powder, which has led to the growth of WS_2 continuous films. Sulfur powder (400 mg of purum grade $\geq$99.5%) was placed in the outer tube at 180 °C, whereas WO_3 powder (200 mg of puriss grade 99.9%) was positioned in the inner tube at 1070 °C. SiO_2/Si (90 nm) substrates were positioned 10 cm downstream of WO_3. An argon flow rate of 250 sccm was used for transporting WO_3 and sulfur vapors to the designated substrates. The growth was initiated by ramping sulfur at ~30 °C/min and WO_3 at ~40 °C/min and giving a 3 min reaction time for domain growth or a 5 min reaction time for continuous film growth after reaching the target reaction temperature (1070 °C). The as-deposited WS_2 samples were quickly cooled as soon as the reaction finished.

Transfer of WS_2 Domains. The as-produced samples were first spin-coated with a PMMA scaffold (8 wt % in anisole, 495k molecular weight) at 4700 rpm for 60 s and then cured at 150 °C for 15 min. The underlying SiO_2/Si substrates were subsequently detached by floating the sample on a 1 M KOH (Sigma-Aldrich reagent grade 90%) solution at room temperature. The floating PMMA/WS_2 films were carefully cleaned by several DI water baths. With regard to the TEM characterization, the PMMA/WS_2 films were transferred onto holey silicon nitride (SiN) TEM grids (Agar Scientific Y5385) and left to dry overnight in air. PMMA/WS_2/SiN was subsequently baked at 150 °C for 15 min to improve sample adhesion. Lastly, TEM samples were prepared by removing PMMA using a 2 h acetone solution bath at 45 °C.

Treatment of WS_2 for GB Optical Imaging. In order to unveil GBs in WS_2 domains and continuous films, the as-prepared WS_2 samples were heated in air by placing them at the center of a Carbolite 1 in. tubular furnace (MTF 12/38A). Samples were removed instantly from the furnace when the treatment was finished and left to cool in air spontaneously. Subsequently, as-treated samples were imaged instantly with the optical microscope at our disposal. In the experiment of an Ar-rich atmosphere for WS_2 GB treatment, we prepared the environment by flushing 500 sccm of Ar for 1 h in a 1 in. quartz tube CVD before ramping up the furnace to 380 °C. The thermal treatment of the WS_2 sample was then carried at 380 °C for 20 min with only 10 sccm of Ar flowing.

Characterization of As-Treated WS_2 Domains. The optical images of WS_2 GBs in domains and films were taken by an eVue Pro 40X digital imaging system lens built for the Cascade MicroTech probe station. A magnification of 5× was used to visualize all aforementioned WS_2 GBs. All as-obtained optical images were brightness/contrast enhanced to improve the presentation of WS_2 GBs using an image processing tool, ImageJ. Raman and photoluminescence characterizations of treated WS_2 domains were conducted using a JY Horiba Labram Aramis imaging confocal Raman microscope at an excitation wavelength of 532 nm. SEM images taken of WS_2 GBs were generated from a Hitachi-4300 scanning electron microscope. Topological characterizations regarding WS_2 GBs were performed using an Asylum Research MFP-3D atomic force microscope. The study of WS_2 GBs regarding TEM SAED patterns was carried using a JEOL 2100 high-resolution TEM operating at 80 kV. The aberration-corrected-TEM images were obtained from Oxford's JEOL JEM-2200MCO field-emission gun TEM, fitted with a CEOS probe, image aberration correctors, and a double Wien Filter monochromator operated at an accelerating voltage of 80 kV. Electrical measurements were conducted on our homemade probe station equipped with two ultrafine tungsten tips (Signatone, SE-T, 5 μm in diameter) and a Keithley source meter (2400-LV). Measurements were all done in room-temperature ambient conditions.

Conflict of Interest: The authors declare no competing financial interest.

Supporting Information Available: A schematic of the CVD system setup. Characteristic Raman and PL intensity profiles for monolayer WS_2 domains and films. Evolution of monolayer WS_2 domains with different durations or temperatures. Monolayer WS_2 domain damage due to further increase of heat treatment temperature or treating duration. Raman and PL 2D mappings for the isolated and conjunctive monolayer WS_2 domains that were not thermally treated. SAED patterns across the WS_2 domains. *IV* source−drain electrical measurements for untreated and treated WS_2 domains and GBs. This material is available free of charge *via* the Internet at http://pubs.acs.org.

Acknowledgment. J.H.W. is thankful for the support from the Royal Society.

REFERENCES AND NOTES

1. Li, X.; Cai, W.; An, J.; Kim, S.; Nah, J.; Yang, D.; Piner, R.; Velamakanni, A.; Jung, I.; Tutuc, E.; *et al.* Large-Area Synthesis of High-Quality and Uniform Graphene Films on Copper Foils. *Science* **2009**, *324*, 1312–1314.
2. Li, X.; Magnuson, C. W.; Venugopal, A.; Tromp, R. M.; Hannon, J. B.; Vogel, E. M.; Colombo, L.; Ruoff, R. S. Large-Area Graphene Single Crystals Grown by Low-Pressure Chemical Vapor Deposition of Methane on Copper. *J. Am. Chem. Soc.* **2011**, *133*, 2816–2819.
3. Bae, S.; Kim, H.; Lee, Y.; Xu, X.; Park, J.; Zheng, Y.; Balakrishnan, J.; Lei, T.; Kim, H. R.; Song, Y. I.; *et al.* Roll-to-Roll Production of 30-in. Graphene Films for Transparent Electrodes. *Nat. Nanotechnol.* **2010**, *5*, 574–578.
4. Zhou, H.; Yu, W. J.; Liu, L.; Cheng, R.; Chen, Y.; Huang, X.; Liu, Y.; Wang, Y.; Huang, Y.; Duan, X. Chemical Vapour Deposition Growth of Large Single Crystals of Monolayer and Bilayer Graphene. *Nat. Commun.* **2013**, *4*, 2096.
5. Wu, Y. A.; Fan, Y.; Speller, S.; Creeth, G. L.; Sadowski, J. T.; He, K.; Robertson, A. W.; Allen, C. S.; Warner, J. H. Large Single Crystals of Graphene on Melted Copper Using Chemical Vapor Deposition. *ACS Nano* **2012**, *6*, 5010–5017.
6. Wu, Y. A.; Robertson, A. W.; Schaeffel, F.; Speller, S. C.; Warner, J. H. Aligned Rectangular Few-Layer Graphene Domains on Copper Surfaces. *Chem. Mater.* **2011**, *23*, 4543–4547.
7. Yu, Q.; Jauregui, L. A.; Wu, W.; Colby, R.; Tian, J.; Su, Z.; Cao, H.; Liu, Z.; Pandey, D.; Wei, D.; *et al.* Control and Characterization of Individual Grains and Grain Boundaries in

Graphene Grown by Chemical Vapour Deposition. *Nat. Mater.* **2011**, *10*, 443–449.
8. van der Zande, A. M.; Huang, P. Y.; Chenet, D. A.; Berkelbach, T. C.; You, Y.; Lee, G.; Heinz, T. F.; Reichman, D. R.; Muller, D. A.; Hone, J. C. Grains and Grain Boundaries in Highly Crystalline Monolayer Molybdenum Disulphide. *Nat. Mater.* **2013**, *12*, 554–561.
9. Yazyev, O. V.; Louie, S. G. Electronic Transport in Polycrystalline Graphene. *Nat. Mater.* **2010**, *9*, 806–809.
10. Najmaei, S.; Amani, M.; Chin, M. L.; Liu, Z.; Birdwell, A. G.; O'Regan, T. P.; Ajayan, P. M.; Dubey, M.; Lou, J. Electrical Transport Properties of Polycrystalline Monolayer Molybdenum Disulfide. *ACS Nano* **2014**, *8*, 7930–7937.
11. Huang, P. Y.; Ruiz-Vargas, C. S.; van der Zande, A. M.; Whitney, W. S.; Levendorf, M. P.; Kevek, J. W.; Garg, S.; Alden, J. S.; Hustedt, C. J.; Zhu, Y.; *et al.* Grains and Grain Boundaries in Single-layer Graphene Atomic Patchwork Quilts. *Nature* **2011**, *469*, 389–392.
12. Kim, K.; Lee, Z.; Regan, W.; Kisielowski, C.; Crommie, M. F.; Zettl, A. Grain Boundary Mapping in Polycrystalline Graphene. *ACS Nano* **2011**, *5*, 2142–2146.
13. Rasool, H. I.; Song, E. B.; Allen, M. J.; Wassei, J. K.; Kaner, R. B.; Wang, K. L.; Weiller, B. H.; Gimzewski, J. K. Continuity of Graphene on Polycrystalline Copper. *Nano Lett.* **2011**, *11*, 251–256.
14. Gao, L.; Guest, J. R.; Guisinger, N. P. Epitaxial Graphene on Cu(111). *Nano Lett.* **2010**, *10*, 3512–3516.
15. Duong, D. L.; Han, G. H.; Lee, S. M.; Gunes, F.; Kim, E. S.; Kim, S. T.; Kim, H.; Ta, Q. H.; So, K. P.; Yoon, S. J.; *et al.* Probing Graphene Grain Boundaries with Optical Microscopy. *Nature* **2012**, *490*, 235–239.
16. Huang, J.; Pu, J.; Hsu, C.; Chiu, M.; Juang, Z.; Chang, Y.; Chang, W.; Iwasa, Y.; Takenobu, T.; Li, L. Large-Area Synthesis of Highly Crystalline WSe_2 Monolayers and Device Applications. *ACS Nano* **2014**, *8*, 923–930.
17. Rong, Y.; Fan, Y.; Koh, A. L.; Robertson, A. W.; He, K.; Wang, S.; Tan, H.; Sinclair, R.; Warner, J. H. Controlling Sulphur Precursor Addition for Large Single Crystal Domains of WS_2. *Nanoscale* **2014**, *6*, 12096–12103.
18. Wang, X.; Gong, Y.; Shi, G.; Chow, W. L.; Keyshar, K.; Ye, G.; Vajtai, R.; Lou, J.; Liu, Z.; Ringe, E.; *et al.* Chemical Vapor Deposition Growth of Crystalline Monolayer $MoSe_2$. *ACS Nano* **2014**, *8*, 5125–5131.
19. Zhang, J.; Yu, H.; Chen, W.; Tian, X.; Liu, D.; Cheng, M.; Xie, G.; Yang, W.; Yang, R.; Bai, X.; *et al.* Scalable Growth of High-Quality Polycrystalline MoS_2 Monolayers on SiO_2 with Tunable Grain Sizes. *ACS Nano* **2014**, *8*, 6024–6030.
20. Lee, Y.; Zhang, X.; Zhang, W.; Chang, M.; Lin, C.; Chang, K.; Yu, Y.; Wang, J. T.; Chang, C.; Li, L.; *et al.* Synthesis of Large-Area MoS_2 Atomic Layers with Chemical Vapor Deposition. *Adv. Mater.* **2012**, *24*, 2320–2325.
21. Chiu, M.; Li, M.; Zhang, W.; Hsu, W.; Chang, W.; Terrones, M.; Terrones, H.; Li, L. Spectroscopic Signatures for Interlayer Coupling in MoS_2-WSe_2 van der Waals Stacking. *ACS Nano* **2014**, *8*, 9649–9656.
22. Ramasubramaniam, A. Large Excitonic Effects in Monolayers of Molybdenum and Tungsten Dichalcogenides. *Phys. Rev. B* **2012**, *86*, 115409.
23. Gutierrez, H. R.; Perea-Lopez, N.; Elias, A. L.; Berkdemir, A.; Wang, B.; Lv, R.; Lopez-Urias, F.; Crespi, V. H.; Terrones, H.; Terrones, M. Extraordinary Room-Temperature Photoluminescence in Triangular WS_2 Monolayers. *Nano Lett.* **2013**, *13*, 3447–3454.
24. Tongay, S.; Fan, W.; Kang, J.; Park, J.; Koldemir, U.; Suh, J.; Narang, D. S.; Liu, K.; Ji, J.; Li, J.; *et al.* Tuning Interlayer Coupling in Large-Area Heterostructures with CVD-Grown MoS_2 and WS_2 Monolayers. *Nano Lett.* **2014**, *14*, 3185–3190.
25. Zhang, W.; Chuu, C.; Huang, J.; Chen, C.; Tsai, M.; Chang, Y.; Liang, C.; Chen, Y.; Chueh, Y.; He, J.; *et al.* Ultrahigh-Gain Photodetectors Based on Atomically Thin Graphene-MoS_2 Heterostructures. *Sci. Rep.* **2014**, *4*, 3826.
26. Zhang, W.; Chiu, M.; Chen, C.; Chen, W.; Li, L.; Wee, A. T. S. Role of Metal Contacts in High-Performance Phototransistors Based on WSe_2 Monolayers. *ACS Nano* **2014**, *8*, 8653–8661.
27. Chang, Y.; Zhang, W.; Zhu, Y.; Han, Y.; Pu, J.; Chang, J.; Hsu, W.; Huang, J.; Hsu, C.; Chiu, M.; *et al.* Monolayer $MoSe_2$ Grown by Chemical Vapor Deposition for Fast Photodetection. *ACS Nano* **2014**, *8*, 8582–8590.
28. Zhang, W.; Huang, J.; Chen, C.; Chang, Y.; Cheng, Y.; Li, L. High-Gain Phototransistors Based on a CVD MoS_2 Monolayer. *Adv. Mater.* **2013**, *25*, 3456–3461.
29. Zhang, Y.; Zhang, Y.; Ji, Q.; Ju, J.; Yuan, H.; Shi, J.; Gao, T.; Ma, D.; Liu, M.; Chen, Y.; *et al.* Controlled Growth of High-Quality Monolayer WS_2 Layers on Sapphire and Imaging Its Grain Boundary. *ACS Nano* **2013**, *7*, 8963–8971.
30. Ly, T. H.; Chiu, M.; Li, M.; Zhao, J.; Perello, D. J.; Cichocka, M. O.; Oh, H. M.; Chae, S. H.; Jeong, H. Y.; Yao, F.; *et al.* Observing Grain Boundaries in CVD-Grown Monolayer Transition Metal Dichalcogenides. *ACS Nano* **2014**, *8*, 11401–11408.
31. Ling, X.; Lee, Y.; Lin, Y.; Fang, W.; Yu, L.; Dresselhaus, M. S.; Kong, J. Role of the Seeding Promoter in MoS_2 Growth by Chemical Vapor Deposition. *Nano Lett.* **2014**, *14*, 464–472.
32. Najmaei, S.; Liu, Z.; Zhou, W.; Zou, X.; Shi, G.; Lei, S.; Yakobson, B. I.; Idrobo, J.; Ajayan, P. M.; Lou, J. Vapour Phase Growth and Grain Boundary Structure of Molybdenum Disulphide Atomic Layers. *Nat. Mater.* **2013**, *12*, 754–759.
33. Nan, H.; Wang, Z.; Wang, W.; Liang, Z.; Lu, Y.; Chen, Q.; He, D.; Tan, P.; Miao, F.; Wang, X.; *et al.* Strong Photoluminescence Enhancement of MoS_2 through Defect Engineering and Oxygen Bonding. *ACS Nano* **2014**, *8*, 5738–5745.
34. Tongay, S.; Zhou, J.; Ataca, C.; Liu, J.; Kang, J. S.; Matthews, T. S.; You, L.; Li, J.; Grossman, J. C.; Wu, J. Broad-Range Modulation of Light Emission in Two-Dimensional Semiconductors by Molecular Physisorption Gating. *Nano Lett.* **2013**, *13*, 2831–2836.
35. Peimyoo, N.; Shang, J.; Cong, C.; Shen, X.; Wu, X.; Yeow, E. K. L.; Yu, T. Nonblinking, Intense Two-Dimensional Light Emitter: Monolayer WS_2 Triangles. *ACS Nano* **2013**, *7*, 10985–10994.
36. Liu, Y.; Ghosh, R.; Wu, D.; Ismach, A.; Ruoff, R.; Lai, K. Mesoscale Imperfections in MoS_2 Atomic Layers Grown by a Vapor Transport Technique. *Nano Lett.* **2014**, *14*, 4682–4686.
37. Zhou, W.; Zou, X.; Najmaei, S.; Liu, Z.; Shi, Y.; Kong, J.; Lou, J.; Ajayan, P. M.; Yakobson, B. I.; Idrobo, J. Intrinsic Structural Defects in Monolayer Molybdenum Disulfide. *Nano Lett.* **2013**, *13*, 2615–2622.